Check for updates

Initialization and read-out of intrinsic spin defects in a van der Waals crystal at room temperature

Andreas Gottscholl[1], Mehran Kianinia[2], Victor Soltamov[1], Sergei Orlinskii[3], Georgy Mamin[3], Carlo Bradac[2], Christian Kasper[1], Klaus Krambrock [4], Andreas Sperlich [1], Milos Toth [2,5], Igor Aharonovich [2,5 ✉] and Vladimir Dyakonov [1 ✉]

Optically addressable spins in wide-bandgap semiconductors are a promising platform for exploring quantum phenomena. While colour centres in three-dimensional crystals such as diamond and silicon carbide were studied in detail, they were not observed experimentally in two-dimensional (2D) materials. Here, we report spin-dependent processes in the 2D material hexagonal boron nitride (hBN). We identify fluorescence lines associated with a particular defect, the negatively charged boron vacancy (V_B^-), showing a triplet ($S = 1$) ground state and zero-field splitting of ~3.5 GHz. We establish that this centre exhibits optically detected magnetic resonance at room temperature and demonstrate its spin polarization under optical pumping, which leads to optically induced population inversion of the spin ground state—a prerequisite for coherent spin-manipulation schemes. Our results constitute a step forward in establishing 2D hBN as a prime platform for scalable quantum technologies, with potential for spin-based quantum information and sensing applications.

The emergence of two-dimensional (2D) materials and van der Waals crystals has enabled the observation and realization of unique optoelectronic and nanophotonic effects, such as Moiré excitons and quantum spin Hall effect at elevated temperatures, to name a few[1,2]. Amidst the large variety of van der Waals crystals studied, hexagonal boron nitride (hBN) offers a combination of unique physical, chemical and optical properties[3]. Most relevant to this work is the ability of hBN to host atomic impurities (or point defects), which give rise to quantized optical transitions that are well below its bandgap[4,5]. hBN colour centres are ultrabright with narrow and tuneable linewidth[6–8], and photostability up to 800 K (ref. [9]). Whilst the nature of many of the defects is still uncertain[10–15], they are being extensively studied as promising candidates for quantum photonic applications requiring on-demand, ultrabright single-photon emission.

A step forward, which will significantly extend the functionality of hBN emitters for quantum applications, is to interface their optical properties with spin transitions, and realize spin polarization and optical spin readout schemes[16,17]. The concept of the spin–photon interface has been extensively studied in quantum dots[18] and the nitrogen vacancy centre in diamond[19]. The latter has been harnessed to realize basic two-node quantum networks[19] and a plethora of advanced quantum-sensing schemes[20–22]. The basic principle is that the high-spin ground or excited state of the defect can be polarized, manipulated and read out optically owing to the spin-dependent excitation, decay and intersystem crossing pathways available to the system during the optical excitation–recombination cycle[23].

Yet, extending the optical control of single-spin states beyond defects in three-dimensional (3D) crystals to those in 2D systems has remained elusive. If achieved, it will open up a range of possibilities both fundamental and technological. The two-dimensional nature of these materials inherently allows for seamless integration with heterogeneous, optoelectronic devices where the hosted solid-state qubits can be readily interfaced with cavities, resonators and nanophotonic components from foreign materials. Further, it naturally grants nanoscale proximity of the spin probe to target samples for high-resolution quantum-sensing realizations. Reliable and deterministic transfer of hBN layers on stacks of other 2D materials is well established and is part of one of the most relevant endeavours of condensed matter physics at present—engineering heterostructures made with purposefully chosen sequences of atomically thin 2D materials[24].

Here, we report on the optical initialization and readout of an ensemble of spins in hBN. We perform rigorous electron paramagnetic resonance (EPR) spectroscopy and optically detected magnetic resonance (ODMR) measurements to establish that the defect has a triplet ground state with a zero-field splitting (ZFS) of ~3.5 GHz and an almost isotropic Landé factor of $g = 2.000$. From the analysis of the angular dependence and nitrogen hyperfine structure, we confirm the intrinsic nature of the defect and assign it to the boron lattice position, which is most likely the negatively charged boron vacancy (V_B^-). The alternative substitutional carbon on a boron site (C_B) or nitrogen vacancy (V_N) structures were also considered, but were discarded upon analysis of the experimental data (see the discussion below).

Figure 1a is a schematic illustration of the proposed defect. The defect is a negatively charged boron vacancy (V_B^-) centre consisting of a missing boron atom surrounded by three equivalent nitrogen atoms in the hBN lattice. The defect has D_{3h} point-group symmetry and exhibits strong room-temperature photoluminescence (PL) emission at $\lambda_{max} \approx 850$ nm under $\lambda_{exc} = 532$ nm laser excitation with an excited-state lifetime of $\tau_{exc} = 1.2$ ns (Fig. 1b). Note that these defects are different to the quantum emitters around 2 eV that were previously investigated[5–8,12].

---

[1]Experimental Physics 6 and Würzburg-Dresden Cluster of Excellence, Julius Maximilian University of Würzburg, Würzburg, Germany. [2]School of Mathematics and Physical Sciences, University of Technology Sydney, Ultimo, New South Wales, Australia. [3]Kazan Federal University, Kazan, Russia. [4]Departamento de Física, Universidade Federal de Minas Gerais, Belo Horizonte, Brazil. [5]ARC Centre of Excellence for Transformative Meta-Optical Systems, University of Technology Sydney, Ultimo, New South Wales, Australia. ✉e-mail: igor.aharonovich@uts.edu.au; vladimir.dyakonov@uni-wuerzburg.de
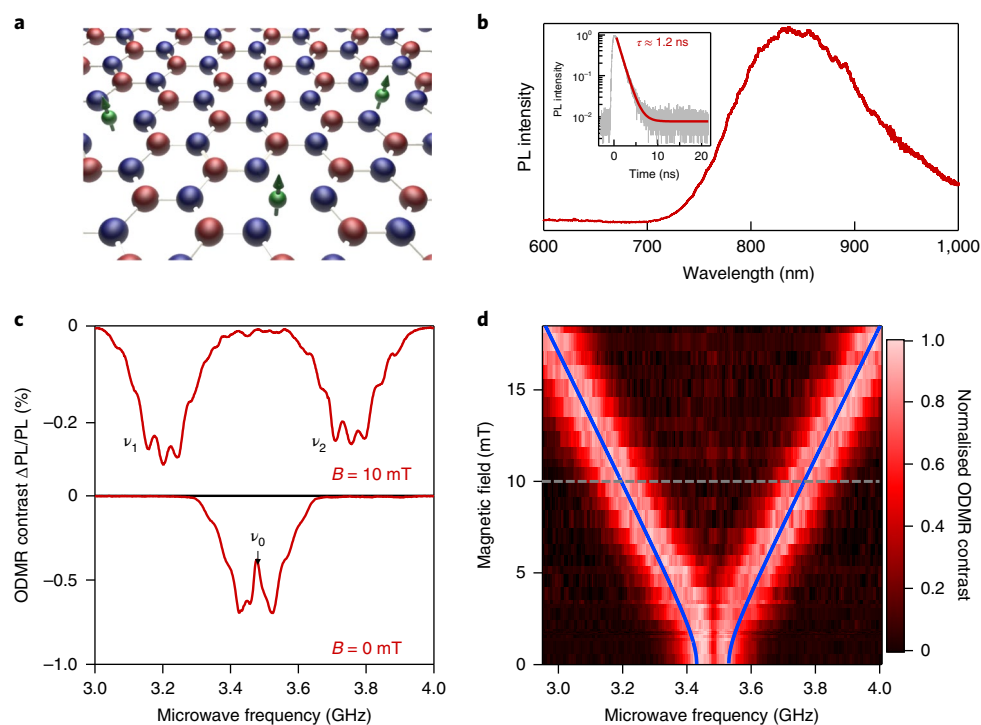
Fig. 1 | ODMR of an hBN single crystal at room temperature, $T = 300$ K. a, Schematic of an hBN monolayer and its crystalline hexagonal structure with alternating boron (red) and nitrogen (blue) atoms. The green arrows indicate the spins of the negatively charged boron vacancy defects, V_B^-. **b**, Photoluminescence spectrum of the sample at room temperature displaying a pronounced emission at 850 nm with excited-state lifetime of $\tau = 1.2$ ns given by fitting (red) the transient PL data (grey) exponentially. **c**, ODMR spectra measured at zero magnetic field (bottom) and at magnetic field $B = 10$ mT (top) with the corresponding ODMR frequencies v_0, v_1 and v_2, respectively. **d**, Dependence of ODMR frequencies on the magnetic field ($\mathbf{B} \parallel \mathbf{c}$). Experimental data (red) and fit (blue line) obtained using equation (2) with parameters $D/h = 3.48$ GHz, $E/h = 50$ MHz and $g = 2.000$. The grey dashed line represents the position of the left ODMR spectrum at $B = 10$ mT.

Most interestingly, we find that the PL from this hBN colour centre is spin dependent. Figure 1c shows the ODMR spectrum recorded for an hBN single crystal at $T = 300$ K. In ODMR experiments, microwave-induced magnetic dipole transitions between spin sublevels manifest as changes in PL intensity (ΔPL). The prerequisite for optical (PL) detection of EPR is thus the existence of a dependence between the optical excitation–recombination cycle and the spin orientation of the defect. Figure 1c shows the spectrum of the investigated sample as normalised change of PL intensity (ΔPL/PL)—that is, ODMR contrast—as a function of the applied microwave frequency v for two static magnetic fields, $B = 0$ and $B = 10$ mT. Even without an external magnetic field, the ODMR spectrum shows two distinct resonances, v_1 and v_2, located symmetrically around the frequency v_0. We tentatively assign them to the $\Delta m_S = \pm 1$ spin transitions between triplet energy sublevels with completely lifted threefold degeneracy, due to a splitting induced by dipolar interaction between the unpaired electron spins, forming the triplet. This so-called zero-field splitting is described by parameters D and E, which can be derived from the spectrum as $D/h = v_0$ and $v_{1,2} = (D \pm E)/h$, with h being Planck's constant, to express the interaction energies in frequency units. To verify this assignment, we have studied the dependence of the v_1 and v_2 resonant microwave frequencies on the magnitude of the external static magnetic field.

The evolution of the ODMR spectrum with the field applied parallel to the hexagonal c axis ($\mathbf{B} \parallel \mathbf{c}$) of hBN is presented in Fig. 1d. To explain the observed transitions and their variation with magnetic field, we use the standard spin Hamiltonian given by equation (1), with Z as the principle symmetry axis oriented perpendicular to the plane (collinear with the c axis of the hBN crystal).

$$H = D(S_z^2 - S(S+1)/3) + E(S_x^2 - S_y^2) + g\mu_B\mathbf{BS} \quad (1)$$

where D and E are the ZFS parameters, $\mathbf{S}$ is the total electron spin ($S = 1$ for triplets), g is the Landé factor, μ_B is the Bohr magneton, $\mathbf{B}$ is the static magnetic field and $S_{x,y,z}$ are the spin-1 operators. According to equation (1), and for $\mathbf{B}$ applied parallel to the c axis, the resonant microwave frequencies at which the transitions occur vary as

$$v_{1,2} = v_0 \pm \frac{1}{h}\sqrt{E^2 + (g\mu_B B)^2} \quad (2)$$

where $v_0 = D/h$. The dependence of ODMR frequencies v_1 and v_2 on the magnetic field shown in Fig. 1d can be perfectly fitted by equation (2) with $g = 2.000$, $D/h = 3.48$ GHz and a small off-axial component of the ZFS $E/h = 50$ MHz. This demonstrates a highly symmetrical, almost uniaxial, defect structure.

So far, we have shown that the investigated hBN defect is an $S = 1$ system, which can be optically addressed and read out using ODMR. From the ODMR measurements alone, however, it is difficult to conclude whether the defect is in an excited, metastable or ground state. It is essential to know this so as to determine the correct spin-dependent recombination pathway. We note that earlier results[25] proposed a defect in hBN with a singlet ground state to possess a spin-triplet metastable state. However, from our EPR results presented below, it becomes clear that we are dealing with another defect here. A second consideration is that zero-field ODMR measurements alone are not sufficient to deduce the microscopic structure of the defect. To address these points, we applied high-field ODMR and EPR to previously studied exfoliated hBN flakes[26],
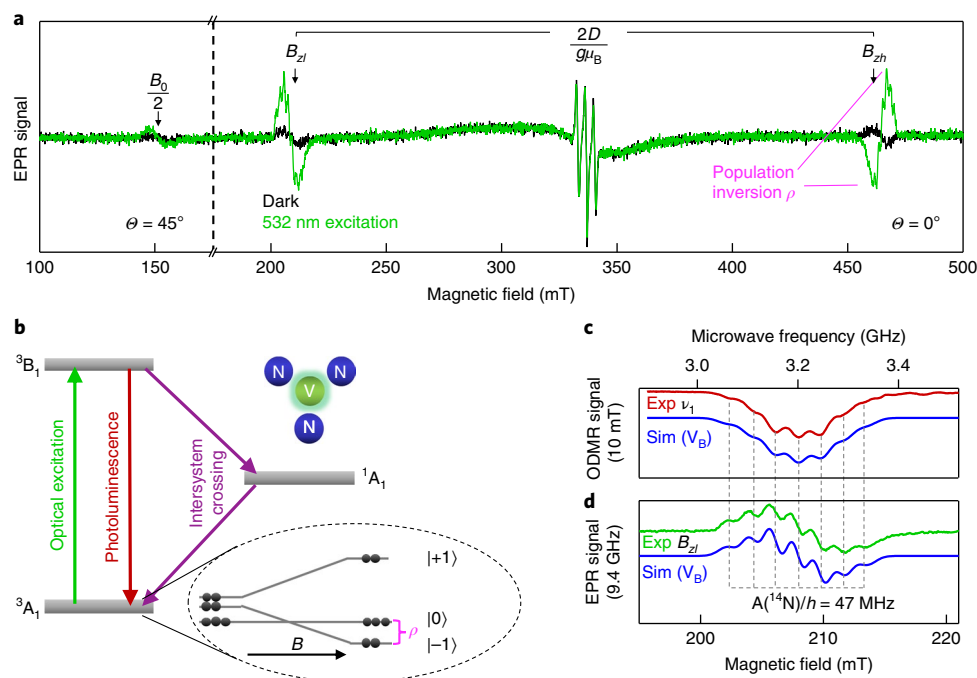
Fig. 2 | X-band EPR studies of the V_B^- centre in the hBN single crystal sample at $T = 5$ K. a, Spectra measured with (green trace) and without (black trace) 532-nm optical excitation in the magnetic field orientation $\Theta = 0°$ (**B** || **c**) and $\Theta = 45°$ to observe the half-field transition $B_0/2$. Doublet lines associated with the $S = 1$ centre with splitting of $\Delta B \approx 260$ mT (equivalent to $2D/h \approx 2 \times 3.6$ GHz) are labelled B_{zl}, B_{zh}. **b**, Simplified energy-level diagram illustrating the optical pump cycle between ground state $^3A_1$, excited state $^3B_1$ and metastable state $^1A_1$ resulting in population inversion, ρ, between $|0\rangle$ and $|-1\rangle$ ground-state spin sublevels. Optical excitation (green), PL (red) and intersystem crossing (purple) are indicated by arrows. V_B^- centre consists of a vacancy (green sphere) surrounded by three nitrogen atoms (blue spheres). **c**, Hyperfine splitting of ODMR ν_1 (red trace) line. **d**, Hyperfine splitting of EPR B_{zl} (green trace) transition. Vertical bars indicate seven transitions caused by hyperfine interaction with three equivalent nitrogen nuclei. The blue traces are the simulated EPR/ODMR spectra of the (V_B^-) defect with equation (1), where the hyperfine term with a splitting constant $A/h = 47$ MHz is considered.

as well as to the hBN single crystal as studied by ODMR and shown in Fig. 1c,d. We also note that defects in hBN single crystals and in the hBN exfoliated flakes were introduced in the same way (see Methods), and we only see the PL emission at 800 nm and ODMR signal after implantation/neutron irradiation. These defects (which may be present) were not optically active in pristine samples.

Figure 2a shows X-band EPR spectra taken at a fixed microwave frequency ($\nu = 9.4$ GHz) while scanning the static magnetic field aligned parallel to the *c* axis of the crystal (**B** || **c**). Due to the amplitude modulation of the *B* field, EPR spectra look like first derivatives of the absorption signals. The spectra are recorded with (green trace) and without (black trace) optical excitation and consist of two groups of signals originating from two different types of paramagnetic species. The first group (centred at $B \approx 330$ mT) is characterized by $g = 2.003$ and consists of three EPR lines of nearly equal intensities corresponding to a paramagnetic centre with electron spin $S = \frac{1}{2}$ interacting with a nuclear spin $I = 1$. The origin of such a splitting is hyperfine interaction. This group of lines remains the same with and without optical excitation and is not observed in ODMR under the same conditions (see Supplementary Fig. 1). So, we conclude that the spin transitions that cause these EPR signals are optically inactive. Although spin $S = \frac{1}{2}$ centres in hBN were reported in the late 1970s and assigned to a one-boron-centre or three-boron-centre defect[27], we believe that we are dealing with an $S = \frac{1}{2}$ centre that occupies a boron site in the lattice that interacts with one ^{14}N ($I = 1$). However, this interpretation is beyond the scope of this work.

On the other hand, the second group of EPR lines in Fig. 2a (labelled B_{zl}, B_{zh} with *l*, *h* indices denoting low and high magnetic field transitions and the principal symmetry axis *Z* the defect orientation **B** || **c** || **Z**) consists of two widely separated transitions, which

are strongly responsive to optical excitation (532 nm laser). The splitting between the lines B_{zl} and B_{zh} ($\Delta B \approx 260$ mT), as well as the position of the $B_0/2$ signals at half-field, is the same as in the ODMR experiments under the same conditions performed on the hBN flakes (see Supplementary Fig. 1). The EPR signals can be satisfyingly described by the spin Hamiltonian (equation (1)) with the following Zeeman and ZFS parameters: $S = 1$, $g = 2.000$, $D/h = 3.6$ GHz. The ZFS parameter *E*, which became apparent in ODMR measurements at $B = 0$ (Fig. 1c), could not be easily resolved in X-band EPR due to its small magnitude. It is, however, noticeable that the EPR measurements yield a slightly larger value for the ground-state ZFS parameter $D/h \approx 3.6$ GHz than we determined from zero-field ODMR. This is expected for triplet spin centres[23] and we attribute this difference to a pronounced temperature dependence of *D* varying between 3.6 GHz at $T = 5$ K (determined via EPR and ODMR) and 3.48 GHz at $T = 300$ K (ODMR). Assuming a linear dependence, this would lead to a slope of approximately 0.4 MHz K^{-1}, which can be reasonably expected for the temperature-induced hBN lattice expansion.

Notably, the phases of the B_{zl} and B_{zh} signals shown in Fig. 2a become opposite (up–down and down–up) upon optical excitation and we observe emission rather than absorption for the EPR transition B_{zh}. This can be explained by an optically induced population inversion ρ taking place amongst the spin-triplet sublevels of the ground state—with either the $m_s = \pm 1$ or $m_s = 0$ sublevels being lower lying at $B = 0$. The order of the energy sublevels $m_s = 0, \pm 1$ is determined by the sign of the ZFS parameter *D*, which is positive in our case ($D > 0$). To prove this independently, we conducted EPR studies without optical excitation and found different signal intensities for B_{zl} and B_{zh} transitions. Figure 3 shows a W-band ($\nu = 94$ GHz) electron spin echo (ESE)-detected EPR spectrum of
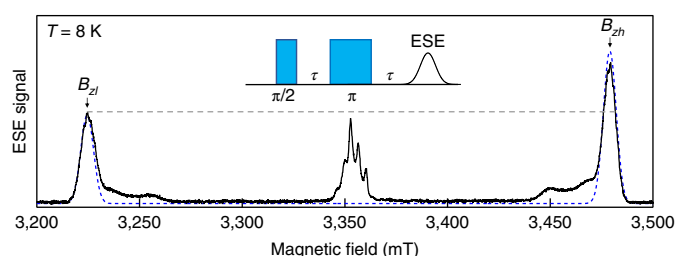
Fig. 3 | Determination of the sign of the ZFS parameter D. Dark W-band EPR spectrum (solid line) and simulation (dashed trace) reproducing the observed intensities (see Methods). The spectrum was recorded using the Hahn echo pulse sequence: $\frac{\pi}{2} - \tau - \pi - \tau - \text{ESE}$ with a $\frac{\pi}{2}$ pulse length of 16 ns and $\tau = 280$ ns. $T = 8$ K.

the hBN single crystal for $\mathbf{B} \approx \| \mathbf{c}$ orientation measured in the dark at $T = 8$ K. The spectrum clearly reveals that the intensity of the low-field transition (B_{Zl}) is lower in magnitude than that of the high-field transition (B_{Zh}). Since the relative magnitudes of the EPR transitions under such experimental conditions are determined only by thermal populations of the Zeeman levels, we can attribute the less intense B_{Zl} EPR line to the transition $m_S = 0 \rightarrow m_S = +1$ and deduce the sign of D to be positive. Schematic comparison of the energetic order of spin sublevels for positive ($D > 0$) and negative ($D < 0$) ZFS and the measurements at different temperatures (25 and 50 K) are shown in Supplementary Fig. 5. This result is in line with ab initio theoretical predictions of D having positive sign in the ground state of the V_B^- defect[28]. Furthermore, the presence of spin echo signals demonstrates that coherent spin manipulation of the V_B^- spin centre is feasible and allows us to estimate the spin coherence time from a Rabi transient recorded at $T = 8$ K to be of the order of 10 μs (see Supplementary Fig. 6).

In Fig. 2b, we propose the tentative energy-level scheme of the spin defect consistent with our observations. Zeeman splitting of the $m_S = \pm 1$ levels results in the crossing of $m_S = -1$ and $m_S = 0$ sublevels, while optical pumping induces population transfer (via excited and metastable states) from $m_S = \pm 1$ to $m_S = 0$, and results in microwave emission at the B_{Zh} field. We also want to emphasize that the EPR transitions between these triplet sublevels are also visible without optical excitation (black trace in Figs. 2a and 3), suggesting that the triplet state we are looking at is in the ground state.

Although hBN can accommodate a large number of defects (either intrinsic or extrinsic) in its lattice sites, the combined EPR and ODMR data allow us to pinpoint the type of defect. The common defects include boron vacancies (V_B), nitrogen vacancies (V_N) and anti-site complexes (for example, a nitrogen atom on a boron site next to a vacancy ($V_N N_B$), or substitutional carbon-related defects, such as C_B or even $V_N C_B$). The complex defects, such as $V_N N_B$ and $V_N C_B$, were shown to have in-plane C_{2v} symmetry[11,29], which is inconsistent with our observations of an almost axial defect with respect to the c axis. On the other hand, it was also shown that point defects V_B, C_B and V_N are characterized by the uniaxial D_{3h} group symmetry, with a C_3 rotation axis parallel to the c axis. These defects are thus compatible with our findings and must be considered. Recent theoretical investigations of point defects in hBN have shown that the neutral V_N^0 and C_B^0 defects should be $S = 1/2$, but they may become non-magnetic in their energetically preferred charge state (V_N^+, V_N^-, C_B^+), while the negatively charged boron vacancy (V_B^-) has been predicted to be stable with an $S = 1$ ground state[30]. In addition, the optically induced spin polarization of the V_B^- triplet ground state through the spin-dependent intersystem crossing pathway has already been theoretically proposed[11].

To discern between possible hBN lattice sites for the defect, we analysed the hyperfine structure of EPR and ODMR signals. Figure 2c shows the B_{Zl} EPR line together with the zero-field ODMR v_1 transition. The hyperfine splitting is known to be due to the interaction of the electron spin with the surrounding nuclear spins, sometimes called superhyperfine interaction—which in turn reflects the nature of the nearest atoms (in our case either three boron or three nitrogen atoms). It can be described by adding the term $\sum_k \mathbf{S} A_k I_k$ to equation (1), where A_k is the hyperfine interaction and I_k is the nuclear spin. The number of observed hyperfine lines is seven (Fig. 2c,d). This is consistent with a spin $S = 1$ point defect localized at the boron site interacting with $n = 3$ equivalent nitrogen atoms (nuclear spin $I = 1$, ^{14}N, 99.63% natural abundance) and it thus supports the cases of the C_B and V_B defects with $2nI + 1 = 7$ hyperfine transitions. Conversely, for V_N there is hyperfine interaction of the electron spin with $n = 3$ equivalent boron atoms, each having two isotopes ($I = 3/2$, ^{11}B, 80.2% natural abundance and $I = 3$, ^{10}B, 19.8% natural abundance), resulting in $2nI + 1 = 10$ plus $2nI + 1 = 19$ transitions. The V_N simulation shown in Supplementary Fig. 2 takes the natural isotope abundance into account and is dominated by the ten hyperfine transitions for ^{11}B.

Consequently, ruling out V_N, the numerical simulations of the hyperfine structure agree well with a carbon atom or a vacancy localized at the boron site (see Fig. 2c,d and Supplementary Fig. 2) yielding a hyperfine splitting constant $A/h = 47$ MHz. Looking more closely, there are no obvious spectral features pointing at hyperfine interactions with second neighbours (boron). These $n = 6$ equivalent boron atoms would have a much smaller coupling constant A with $2nI + 1 = 20$ plus 38 transitions for ^{10}B and ^{11}B, respectively. The spectral features would fall within the observed linewidth and would only result in slight broadening and miniscule modulations on top of the spectrum. Alternatively, the lack of obvious second-neighbour hyperfine interaction could be a sign of a very localized wavefunction. Future simulations, in combination with electron nuclear double resonance experiments, could help to clarify the wavefunction extent.

Note that while we can determine the defect symmetry (D_{3h}) and lattice site (boron) on the basis of EPR data alone, we cannot fully discern whether the defect is intrinsic (V_B) or extrinsic (C_B). Consequently, we performed irradiation of pristine hBN material (see Methods) with various species: ion implantation with different ions (lithium and gallium) on hBN flakes, as well as neutron irradiation on exfoliated flakes and an hBN single crystal. The 800-nm PL band (Fig. 1b) can be observed for all of these samples (Supplementary Fig. 4a). Furthermore, ODMR is detected (Supplementary Figs. 1 and 4b) for all but the gallium-implanted flakes, due to damage from the gallium beam and very low PL intensity to yield an ODMR contrast. We can thus deduce that the investigated defect is indeed of intrinsic nature and is most likely the V_B^-.

To test the symmetry of the defect more closely we analysed the angular dependencies of the EPR signals for rotations around the polar and azimuthal angles Θ and Φ, respectively. Figure 4 shows the EPR signals measured for a polar rotation (Θ) of the magnetic field from parallel ($\mathbf{B} \| \mathbf{c}$) to perpendicular ($\mathbf{B} \perp \mathbf{c}$) orientation and for azimuthal rotation (Φ) in the (0001) plane ($\mathbf{B} \perp \mathbf{c}$) of an hBN single crystal. The angular variation of the resonant magnetic fields is described by numerical simulation (shown with blue traces in Fig. 4b,d) of equation (1) employing the full set of the previously derived parameters (S, g, D, E), as summarized in Supplementary Table 1. For both polar (Fig. 4a) and azimuthal rotation (Fig. 4b) we find exceptionally good agreement of the overlaid simulated traces and the magnetic field positions of the experimentally observed transitions. We note that for the angular dependence shown in Fig. 4d the splitting between the lines remains unchanged. These results point at the c axis being the axis of symmetry of the almost uniaxial ODMR active triplet.
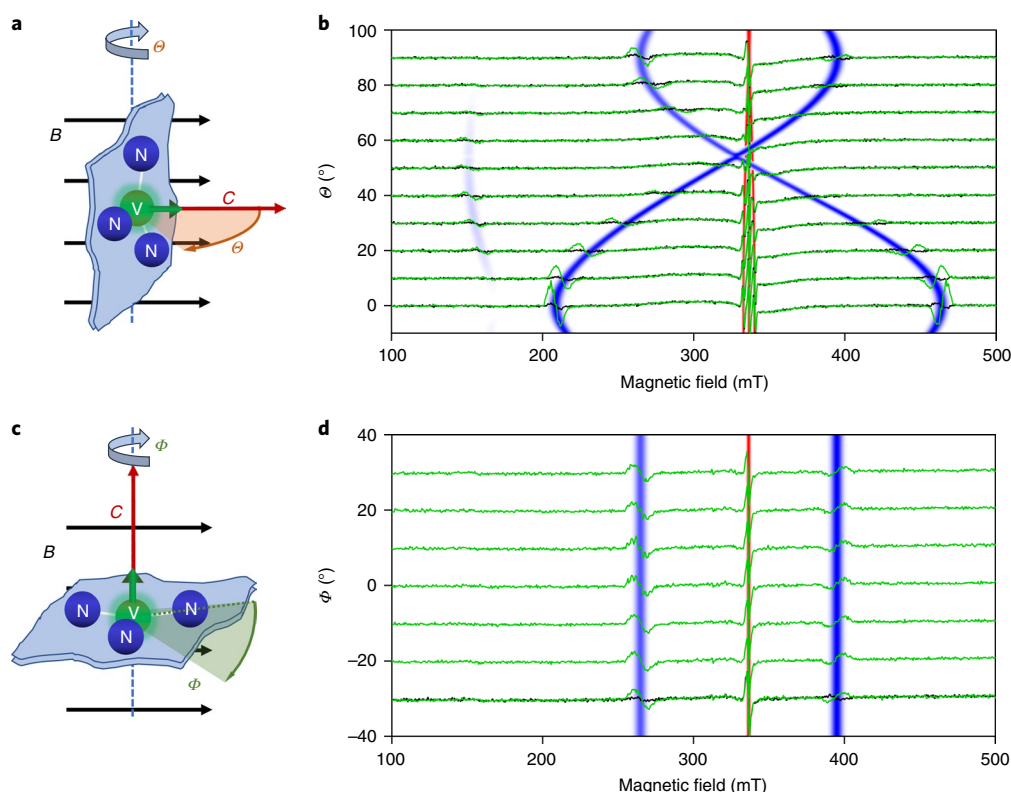
Fig. 4 | Angular dependence of EPR spectra (green traces) and simulations (blue traces) in hBN single crystal. a–d, V_B^- centre consists of a vacancy (green sphere) surrounded by three nitrogen atoms (blue spheres). **a,b**, Rotation of the magnetic field **B** (black arrows) relative to the c axis (red arrow) by angle Θ from parallel ($\Theta = 0°$, **B** || **c**) to perpendicular ($\Theta = 90°$, **B** ⊥ **c**) orientation (**a**) with resulting EPR spectra (**b**). **c,d**, Rotation of the magnetic field **B** (black arrows) by angle Φ in the (0001) plane of hBN (**B** ⊥ **c**) (**c**) with resulting EPR spectra (**d**). Angular variation of the $S = 1/2$ centre (central EPR group, see text) is shown in red. The detailed analysis of this region is shown in Supplementary Fig. 3.

To conclude, we have demonstrated room-temperature optical initialization and readout of ensembles of intrinsic $S = 1$ defect centres in hBN. From rigorous EPR measurements performed on hBN single crystal, exfoliated and ion-irradiated flakes, we propose that the investigated defect is the negatively charged boron vacancy V_B^-. We further demonstrated spin polarization under optical excitation and optically induced population inversion in the triplet ground state, which provides the basis for coherent spin manipulation. While the research into spin defects always starts with ensembles, we are confident that in the future it will be possible to address individual V_B^- defects, particularly using super-resolution techniques[31]. The main challenge lies in the means to increase the quantum efficiency and engineer defects deterministically at various densities. One particularly promising approach is to use resonant excitation to select one or a few defects out of an ensemble, at cryogenic temperatures[32]. This stimulates further research in hBN-based heterostructures for quantum-sensing applications and drives interest into deterministically engineering single V_B^- centres. The work will also accelerate the research into spin optomechanics with hBN, particularly given the established theoretical framework[33] and advances in nanofabrication of resonators[34]. The very fact that spin echo experiments were possible on hBN clearly proves that we are dealing with a coherent spin system characterized by a spin–spin coherence time that is long enough for coherent spin manipulation by microwave fields. The spin–spin coherence time at cryogenic temperatures can be estimated to be several microseconds and is limited by the nuclear bath, in particular by boron nuclei with high gyromagnetic ratio, so that isotopic purification in hBN will be necessary. As reported, isotope purification of 2D materials is much easier than for conventional 3D systems and coherent manipulation of spin states may become feasible, yielding potentially high coherence time[35]. In this context, the V_B^- defect identified here may be advantageous due to weaker coupling of the defect electron spin with the surrounding ^{14}N nuclear bath compared to other possible defect configurations.

Online content
Any methods, additional references, Nature Research reporting summaries, source data, extended data, supplementary information, acknowledgements, peer review information; details of author contributions and competing interests; and statements of data and code availability are available at https://doi.org/10.1038/s41563-020-0619-6.

References
1. Qian, X., Liu, J., Fu, L. & Li, J. Quantum spin Hall effect in two-dimensional transition metal dichalcogenides. *Science* **346**, 1344–1347 (2014).
2. Urbaszek, B. & Srivastava, A. Materials in flatland twist and shine. *Nature* **567**, 39–40 (2019).
3. Caldwell, J. D. et al. Photonics with hexagonal boron nitride. *Nat. Rev. Mater.* **4**, 552–567 (2019).
4. Toth, M. & Aharonovich, I. Single photon sources in atomically thin materials. *Annu. Rev. Phys. Chem.* **70**, 132–142 (2019).
5. Tran, T. T., Bray, K., Ford, M. J., Toth, M. & Aharonovich, I. Quantum emission from hexagonal boron nitride monolayers. *Nat. Nanotechnol.* **11**, 37–41 (2016).
6. Tran, T. T. et al. Robust multicolor single photon emission from point defects in hexagonal boron nitride. *ACS Nano* **10**, 7331–7338 (2016).

7. Jungwirth, N. R. et al. Temperature dependence of wavelength selectable zero-phonon emission from single defects in hexagonal boron nitride. *Nano Lett.* **16**, 6052–6057 (2016).
8. Shotan, Z. et al. Photoinduced modification of single-photon emitters in hexagonal boron nitride. *ACS Photonics* **3**, 2490–2496 (2016).
9. Kianinia, M. et al. Robust solid-state quantum system operating at 800 K. *ACS Photonics* **4**, 768–773 (2017).
10. Tawfik, S. A. et al. First-principles investigation of quantum emission from hBN defects. *Nanoscale* **9**, 13575–13582 (2017).
11. Abdi, M., Chou, J.-P., Gali, A. & Plenio, M. B. Color centers in hexagonal boron nitride monolayers: a group theory and ab initio analysis. *ACS Photonics* **5**, 1967–1976 (2018).
12. Vogl, T., Campbell, G., Buchler, B. C., Lu, Y. & Lam, P. K. Fabrication and deterministic transfer of high-quality quantum emitters in hexagonal boron nitride. *ACS Photonics* **5**, 2305–2312 (2018).
13. Proscia, N. V. et al. Near-deterministic activation of room temperature quantum emitters in hexagonal boron nitride. *Optica* **5**, 1128–1134 (2018).
14. Li, X. et al. Nonmagnetic quantum emitters in boron nitride with ultranarrow and sideband-free emission spectra. *ACS Nano* **11**, 6652–6660 (2017).
15. Exarhos, A. L., Hopper, D. A., Grote, R. R., Alkauskas, A. & Bassett, L. C. Optical signatures of quantum emitters in suspended hexagonal boron nitride. *ACS Nano* **11**, 3328–3336 (2017).
16. Atatüre, M., Englund, D., Vamivakas, N., Lee, S.-Y. & Wrachtrup, J. Material platforms for spin-based photonic quantum technologies. *Nat. Rev. Mater.* **3**, 38–51 (2018).
17. Gao, W. B., Imamoglu, A., Bernien, H. & Hanson, R. Coherent manipulation, measurement and entanglement of individual solid-state spins using optical fields. *Nat. Photonics* **9**, 363–373 (2015).
18. Yılmaz, S. T., Fallahi, P. & Imamoğlu, A. Quantum-dot-spin single-photon interface. *Phys. Rev. Lett.* **105**, 033601 (2010).
19. Kalb, N. et al. Entanglement distillation between solid-state quantum network nodes. *Science* **356**, 928–932 (2017).
20. Mamin, H. J. et al. Nanoscale nuclear magnetic resonance with a nitrogen-vacancy spin sensor. *Science* **339**, 557–560 (2013).
21. Aslam, N. et al. Nanoscale nuclear magnetic resonance with chemical resolution. *Science* **357**, 67–71 (2017).
22. Lovchinsky, I. et al. Nuclear magnetic resonance detection and spectroscopy of single proteins using quantum logic. *Science* **351**, 836–841 (2016).
23. Doherty, M. W. et al. The nitrogen-vacancy colour centre in diamond. *Phys. Rep.* **528**, 1–45 (2013).
24. Geim, A. K. & Grigorieva, I. V. Van der Waals heterostructures. *Nature* **499**, 419–425 (2013).
25. Exarhos, A. L., Hopper, D. A., Patel, R. N., Doherty, M. W. & Bassett, L. C. Magnetic-field-dependent quantum emission in hexagonal boron nitride at room temperature. *Nat. Commun.* **10**, 222 (2019).
26. Toledo, J. R. et al. Electron paramagnetic resonance signature of point defects in neutron-irradiated hexagonal boron nitride. *Phys. Rev. B* **98**, 155203 (2018).
27. Katzir, A., Suss, J. T., Zunger, A. & Halperin, A. Point defects in hexagonal boron nitride. I. EPR, thermoluminescence, and thermally-stimulated-current measurements. *Phys. Rev. B* **11**, 2370–2377 (1975).
28. Ivády, V. et al. Ab initio theory of negatively charged boron vacancy qubit in hBN. Preprint at https://arxiv.org/abs/1910.07767 (2019).
29. Huang, B., Xiang, H., Yu, J. & Wei, S.-H. Effective control of the charge and magnetic states of transition-metal atoms on single-layer boron nitride. *Phys. Rev. Lett.* **108**, 206802 (2012).
30. Weston, L., Wickramaratne, D., Mackoit, M., Alkauskas, A. & van de Walle, C. G. Native point defects and impurities in hexagonal boron nitride. *Phys. Rev. B* **97**, 214104 (2018).
31. Feng, J. et al. Imaging of optically active defects with nanometer resolution. *Nano Lett.* **18**, 1739–1744 (2018).
32. Dietrich, A. et al. Observation of Fourier transform limited lines in hexagonal boron nitride. *Phys. Rev. B* **98**, 081414 (2018).
33. Abdi, M., Hwang, M.-J., Aghtar, M. & Plenio, M. B. Spin-mechanical scheme with color centers in hexagonal boron nitride membranes. *Phys. Rev. Lett.* **119**, 233602 (2017).
34. Shandilya, P. K. et al. Hexagonal boron nitride cavity optomechanics. *Nano Lett.* **19**, 1343–1350 (2019).
35. Ye, M., Seo, H. & Galli, G. Spin coherence in two-dimensional materials. *npj Comput. Mater.* **5**, 44 (2019).

Methods

hBN samples. Monocrystalline hBN and exfoliated flakes from graphene (HQ Graphene) were neutron irradiated in the Triga Mark I IPR-R1 nuclear reactor (CDTN, Brazil), with a thermal flux of $4 \times 10^{12}\,n\,cm^{-2}\,s^{-1}$ for 16 h reaching an integrated dose of approximately $2.3 \times 10^{18}\,n\,cm^{-2}$. All the samples were irradiated in cadmium capsules in which thermal neutrons are blocked, whilst the most energetic neutrons pass through the sample. The multilayered hBN flakes were irradiated with lithium or gallium ions, respectively, to create the defects. The same luminescence features were observed after neutron irradiation, as well as lithium or gallium ion implantation (see Supplementary Fig. 4a). Irradiation of the pristine hBN samples with different sources was conducted to test our hypothesis that the emitters are intrinsic in nature rather than due to inclusion of foreign atoms. Irrespective of the source, the same luminescence emission appears in the near-infrared when the irradiated samples are excited with a green laser, similar to the one presented in Fig. 1b. For more details about sample preparation by fast neutrons and thermal stability of produced defects see ref. [26].

Zero-field ODMR. The zero-field ODMR measurements were performed with a confocal microscope set-up. For optical excitation, a 532-nm laser was coupled into a 50-μm optical fibre and focused onto the sample using a ×10 objective (Olympus LMPLN10XIR), with the laser spot measuring approximately 10 μm in diameter. The laser power at the surface of the sample was 10 mW. The PL was then collected through the same objective and separated from the scattered laser light using a 650-nm short-pass dichroic mirror and a 532-nm long-pass filter. Behind the filter, the PL was coupled into a 600-μm optical fibre and detected using a silicon avalanche photodiode (Thorlabs APD120A). The sample was placed on a 0.5-mm-wide copper stripline to apply the microwaves generated by a signal generator (Stanford Research Systems SG384) and amplified (Mini Circuits ZVE-3W-83+ amplifier). ODMR was detected by a Signal Recovery 7230 lock-in amplifier referenced by on–off modulation of the microwaves. A permanent magnet was mounted below the sample to generate the external magnetic field.

EPR measurements. X-Band ($\nu = 9.4\,GHz$) EPR measurements were carried out with a modified Bruker spectrometer with a microwave power of 20 μW ($B_1 \approx 0.5\,\mu T$). The hBN sample was placed inside an optically accessible microwave cavity on a rotatable quartz rod to change the angle with respect to the external magnetic field. Using an Oxford cryostat, the sample was cooled down to 5 K. For optical excitation, a 532-nm laser with 50 mW of power was directed through an optical window of the cavity. W-Band ($\nu = 94\,GHz$), pulsed EPR measurements were carried out with a Bruker Elexsys 680 spectrometer equipped with an Oxford helium flow cryostat operating in a temperature range of 8 K–300 K. ESE-detected EPR spectra were recorded using a standard Hahn echo pulse sequence: $\frac{\pi}{2} - \tau - \pi - \tau - ESE$ with a $\frac{\pi}{2}$ pulse length of 16 ns and $\tau = 280\,ns$.

High-field ODMR. X-Band ($\nu = 9.4\,GHz$) ODMR measurements were performed in the same set-up as for EPR using a second cavity window for optical readout. Transmitted light of the excitation wavelength was blocked by two filters (550 nm and 561 nm long pass) to detect the remaining broad PL of the emitting defects with a silicon photodiode (Hamamatsu S2281). The microwave source (Anritsu) was on–off modulated with 787 Hz and amplified to 2 W. The PL signal was pre-amplified (Femto DLCPA-200) and recorded by a lock-in amplifier (Signal Recovery 7230). All EPR/ODMR spectral simulations were performed using EasySpin[36].

Data availability

The raw data supporting the findings of this study are available from the corresponding authors upon request.

References

36. Stoll, S. & Schweiger, A. EasySpin, a comprehensive software package for spectral simulation and analysis in EPR. *J. Magn. Reson.* **178**, 42–55 (2006).

Author contributions

The experimental set-ups were implemented and the PL, X-EPR and ODMR measurements were performed by A.G., C.K., K.K., M.K., C.B., A.S. and V.S. I.A., M.K., C.B. and M.T. fabricated the samples and performed optical characterization. K.K. performed neutron irradiation. S.O., G.M. and V.S. performed pulsed EPR experiments. V.D. and I.A. conceived and supervised the project. All the authors contributed to analysis of the data, discussions and to the writing of the paper.

Competing interests

The authors declare no competing interests.

Additional information

Supplementary information is available for this paper at https://doi.org/10.1038/s41563-020-0619-6.

Correspondence and requests for materials should be addressed to I.A. or V.D.

Reprints and permissions information is available at www.nature.com/reprints.